Idealized Modeling of Convective Organization with Changing Sea Surface Temperatures Using Multiple Equilibria in Weak Temperature Gradient Simulations

Stipo Sentić[1], and Sharon L. Sessions[1]

Corresponding author: S. Sentić, Physics Department and Geophysical Research Center, New Mexico Institute of Mining and Technology, 801 Leroy Place, Socorro, NM 87801, USA. (stipo.sentic@student.nmt.edu)

[1]Physics Department and Geophysical Research Center, New Mexico Institute of Mining and Technology, 801 Leroy Place, Socorro, NM 87801, USA.

Abstract.

The weak temperature gradient (WTG) approximation is a method of parameterizing the influences of the large-scale on local convection in limited domain simulations. WTG simulations exhibit multiple equilibria in precipitation; depending on the initial moisture content, simulations can precipitate or remain dry for otherwise identical boundary conditions. We use a hypothesized analogy between multiple equilibria in precipitation in WTG simulations, and dry and moist regions of organized convection to study tropical convective organization.

We find that the range of wind speeds that support multiple equilibria depends on sea surface temperature (SST). Compared to the present SST, low SSTs support a narrower range of multiple equilibria at higher wind speeds. In contrast, high SSTs exhibit a narrower range of multiple equilibria at low wind speeds. This suggests that at high SSTs, organized convection might occur with lower surface forcing.

In order to characterize convection at different SSTs, we analyze the change in relationships between precipitation rate, atmospheric stability, moisture content, and the large-scale transport of moist entropy and moisture with increasing SSTs. We find an increase in large-scale export of moisture and moist entropy from dry simulations with increasing SST, which is consistent with a strengthening of the up-gradient transport of moisture from dry regions to moist regions in organized convection. Furthermore, the changes in

diagnostic relationships with SST are consistent with more intense convection in precipitating regions of organized convection for higher SSTs.

Three key points:

At high SSTs, convective organization occurs at lower wind speeds compared to low SSTs.

The largest range of wind speeds supporting convective organization occurs with an SST of 300 K.

Convective diagnostics show a strengthening of convection at higher SSTs in precipitating regions of organized convection.

1. Introduction

Tropical convective organization is a process in which disorganized, scattered convection organizes into intensely precipitating regions surrounded by dry, non-precipitating regions. Convective organization regulates the atmospheric energy budget, and modulates the strength of severe and intraseasonal weather (e.g. hurricanes and the Madden-Julian Oscillation); understanding convective organization in a changing climate can help us improve weather prediction models. Organized convection cools the atmosphere relative to unorganized convection[*Bretherton et al.*, 2005; *Wing and Emanuel*, 2013; *Muller and Held*, 2012; *Tobin et al.*, 2012]—with more outgoing long-wave radiation, lower albedo, and fewer clouds.

Convection is known to organize and to initiate tropical cyclogenesis under forcing by disturbances such as Easterly waves [*Thorncroft and Hodges*, 2001], Kelvin waves, and the Madden Julian Oscillation [MJO, *Schreck III*, 2015]. However, recent numerical results [*Bretherton et al.*, 2005; *Muller and Held*, 2012; *Wing and Emanuel*, 2013] suggest that convective organization might occur without an apparent external forcing; radiative convective equilibrium (RCE) simulations spontaneously form organized regions of convection surrounded by dry regions—colloquially referred to as "self-aggregation". This spontaneous convective organization occurs at a wide range of sea surface temperatures [SSTs, *Wing and Emanuel*, 2013; *Coppin and Bony*, 2015]. Understanding spontaneous convective organization in the context of changing SSTs can help in better predicting thermodynamic budgets and future climate states.

Recent advances in modeling tropical convection offer tools for studying convective organization in a changing climate in an idealized manner. One such tool is the weak temperature gradient (WTG) approximation [*Sobel and Bretherton*, 2000; *Raymond and Zeng*, 2005; *Herman and Raymond*, 2014]. Based on the observed weak horizontal temperature gradients in the tropics, the WTG approximation parameterizes the effects of the large-scale in limited domain simulations, and it is used to study the effects of changes in the large-scale temperature and moisture on local convection [*Sobel and Bretherton*, 2000; *Raymond and Zeng*, 2005; *Raymond and Sessions*, 2007; *Sessions et al.*, 2015, 2016]. Additionally, the WTG approximation allows for decoupling of dynamic and thermodynamic forcing to study their isolated effects on convection. For instance, researchers have studied the convective response to radiation [*Anber et al.*, 2014, 2015; *Wang et al.*, 2013, 2015; *Sessions et al.*, 2016], moisture treatment [*Wang and Sobel*, 2012; *Sessions et al.*, 2015], surface fluxes [*Raymond and Zeng*, 2005; *Sessions et al.*, 2010; *Anber et al.*, 2015], vertical wind shear [*Anber et al.*, 2014, 2015], SSTs [*Sobel and Bretherton*, 2000; *Wang and Sobel*, 2011; *Daleu et al.*, 2016], and changes in atmospheric stability and moisture [*Raymond and Sessions*, 2007; *Sessions et al.*, 2015, 2016]. The WTG approximation has also been applied to modeling the evolution of the thermodynamic environment in tropical cyclogenesis [*Raymond and Sessions*, 2007] and the Madden Julian Oscillation [*Wang et al.*, 2013, 2015; *Sentić et al.*, 2015], both known instances of convective organization.

The WTG approximation can be used for studying convective organization by utilizing the hypothesized analogy [*Emanuel et al.*, 2014; *Anber et al.*, 2014; *Sessions et al.*, 2015, 2016] between the moist and dry regions in domains with organized convection and multiple equilibria in precipitation exhibited in WTG simulations [*Raymond and Zeng*,

2005; *Sessions et al.*, 2010; *Anber et al.*, 2014; *Herman and Raymond*, 2014; *Sessions et al.*, 2015, 2016]. Multiple equilibria in precipitation are defined as a dry or moist steady state for given boundary conditions when the domain is initialized dry or moist [e.g., *Sobel et al.*, 2007; *Sessions et al.*, 2010]. In this paper, we study the SST dependence of multiple equilibria in precipitation in WTG simulations as an analogue to organized convection. First we determine if the range of multiple equilibria changes with SST to determine whether conditions supporting organized convection change with SST. Second, we diagnose the precipitating and non-precipitating equilibria, and quantify diagnostic relationships to assess how the equilibria change with changing SSTs. Previous research studied the precipitation-saturation fraction relationship as a function of SST for satellite observations [*Peters and Neelin*, 2006]. Here, we study how that and other diagnostic relationships, relevant to convective organization and WTG multiple equlibria, change with SST for the tropical atmosphere.

This paper is organized as follows. In section 2, we describe the cloud resolving model, the WTG approximation, the diagnostic variables, and the methodology used in this study. Section 3 describes the RCE simulations used in obtaining reference profiles for the WTG simulations, while section 4 examines multiple equilibria in precipitation in WTG simulations. Section 5 diagnoses convection and multiple equilibria at the 300 K SST, while section 6 summarizes the influence of changing SSTs on dry and precipitating regions of organized convection. In section 7 we summarize our results and conclusions.

2. Model and methodology

2.1. Cloud resolving model and the weak temperature gradient approximation

A full description of the cloud resolving model used in this study can be found in *Herman and Raymond* [2014]; *Sessions et al.* [2015]; *Sentić et al.* [2015]. The model solves in tandem the fully-compressible non-hydrostatic Navier-Stokes equations, the total water vapor mixing ratio, and the moist entropy equation (moist entropy is related to the equivalent potential temperature). The model achieves radiative convective equilibrium (RCE) in the absence of interactions with the large-scale environment. To parameterize the effects of large-scale environments on local convection we use the relaxed spectral weak temperature gradient (WTG) approximation [*Herman and Raymond*, 2014].

The WTG approximation is based on the assumption that gravity waves redistribute heating anomalies that arise due to diabatic heating [*Bretherton and Smolarkiewicz*, 1989]. The redistributed energy causes adiabatic lifting of surrounding parcels via the vertical WTG mass transfer ρw_{WTG}, where ρ is the domain mean density, and w_{WTG} is the vertical WTG velocity. For a detailed explanation on how the vertical WTG velocity is calculated, please see *Herman and Raymond* [2014]. The WTG approximation assumes that the heating anomaly redistributes over the domain over a timescale τ, which is related to the vertical wave-number of the gravity waves which redistribute the heating anomalies. Conversely, the timescale can be associated with the spatial scale, L, over which the heating anomaly is redistributed. In this study, we used $\tau = 1$ h for the base vertical wave-number, which corresponds to $L = 171.8$ km. The WTG vertical velocity is applied to the thermodynamic (moist entropy and total water vapor mixing ratio) equations through which the model communicates with the reference environment.

Please see *Herman and Raymond* [2014]; *Sessions et al.* [2015], or *Sentić et al.* [2015] for technical details of the implementation of the WTG approximation in the CRM.

2.2. Overall approach

We use the interactive simplified radiative cooling parameterization of *Raymond* [2001, with a solar constant of 1360 W m^{-2}], where water vapor is used as the only active species in the longwave radiative transfer model, with simplified shortwave cloud interactions, and with greenhouse gas concentrations fixed. The radiation scheme compares well qualitatively to the rapid radiative transfer model (RRTM) radiation package [*Mlawer et al.*, 1997] over the range of SSTs used in this study (not shown). Research shows that interactive radiation is conducive and in many models necessary to produce convective organization [*Muller and Held*, 2012; *Emanuel et al.*, 2014; *Sessions et al.*, 2016], and that WTG experiments using static radiative profiles hinder organization [*Sessions et al.*, 2016]. Our choice of interactive radiation is based on *Sessions et al.* [2016], who showed that interactive radiative cooling produces a larger range of multiple equilibria in WTG simulations.

Changes in the climate are parameterized via changes in SSTs, and consequently in changes in surface fluxes. We use a bulk surface entropy flux parameterization:

$$S_{ss} = C_d U_e (s_{ss} - s(0))b, \tag{1}$$

$$S_{rs} = C_d U_e (r_{ss} - r_t(0))b, \tag{2}$$

where S_{ss} and S_{rs} are the bulk surface sources of entropy and total water vapor mixing ratio, respectively, C_d is the transfer coefficient, $U_e = (u(0)^2 + v(0)^2 + W^2)^{1/2}$ is the effective surface wind speed, $W = 3$ m s^{-1} the minimal effective surface wind speed, $u(0)$

and $v(0)$ the components of the surface wind speed, s_{ss} and r_{ss} are the saturated sea surface entropy and total water vapor mixing ratio, respectively, and $s(0)$ and $r_t(0)$ are the surface entropy and total water vapor mixing ratio, respectively. The coefficient b is a numerical constant associated with the deposition of the fluxes in a staggered model grid. The CRM local domain winds are interactive; however, they are relaxed to imposed values of shear-free horizontal wind speed over a relaxation scale $d_r = 5 \cdot 10^{-5}$ s^{-1}; the imposed wind speed varies from 0 to 20 m s^{-1}.

We use two-dimensional model domains; *Wang and Sobel* [2011] showed that compared to three-dimensional simulations, two-dimensional simulations are warmer and moister. Since we compare our results with current findings qualitatively, two-dimensional simulations are sufficient. Also, since we are using small two-dimensional domains in our simulations, the RCE simulations used to produce reference profiles cannot self-aggregate as in other studies of organization of convection [e.g., as in *Wing and Emanuel*, 2013]. In this study we use two-dimensional domains 200 km by 20 km in the horizontal and vertical, respectively, with 1 km horizontal, and 250 m vertical resolution.

A wide range of SSTs, from as low as 280K, up to 310 K SST, has been used in recent studies of organized convection [*Wing and Emanuel*, 2013; *Coppin and Bony*, 2015; *Wing and Cronin*, 2016], and studies of the energetics of the tropical atmosphere [*Singh and O'Gorman*, 2013, 2015, 2016], which far exceed the projected temperature changes from current climate models. *Emanuel et al.* [2014] found that the current SSTs might be associated with a critical response of the atmosphere, which might cause large sensitivities in organized convection for small changes in SSTs. The authors proposed to extend the SSTs in studies of tropical convection far beyond the current value to minimize the influence

of model sensitivity on results. As a consequence of this approach researchers have found that different mechanisms influence convective organization differently at different SSTs [*Abbot*, 2014; *Coppin and Bony*, 2015; *Holloway and Woolnough*, 2016]. We also use a wide range of SSTs (see section 2.4) in our study of organized convection, in order to quantify the sensitivity of different diagnostics to SST changes.

2.3. Diagnostic variables

In this paper, we investigate how the dry and moist equilibria in precipitation change with SST by quantifying changes in precipitation rate, saturation fraction, instability index, deep convective inhibition (DCIN), and normalized gross moist stability (NGMS).

The precipitation rate is a direct measure of convective activity, and is used to directly diagnose the dry and moist equilibrium states, while saturation fraction, defined as precipitable water divided by saturated precipitable water, quantifies moisture content. Saturation fraction can be thought of as a column relative humidity. A number of studies have found an increase in precipitation rate with increasing saturation fraction [*Bretherton et al.*, 2004; *Peters and Neelin*, 2006; *Raymond*, 2007].

Instability index is a temperature dependent diagnostic defined as the difference between the average saturated moist entropy between 1 and 3 km and 5 and 7 km; a smaller but positive instability index corresponds to a more stable atmosphere but still unstable to moist convection. WTG simulations of the tropical atmosphere [*Raymond and Sessions*, 2007; *Raymond and Flores*, 2016a] and observations [*Gjorgjievska and Raymond*, 2014; *Sentić et al.*, 2015; *Raymond and Flores*, 2016a] have shown that a decrease in the instability index results in a more bottom heavy mass flux profile which concentrates moisture convergence at lowest, most moist, levels, which increases saturation fraction and therefore

precipitation rate [*Raymond and Sessions*, 2007; *Sessions et al.*, 2015; *Sentić et al.*, 2015]. This mechanism is hypothesized to play a role in convective organization [*Gjorgjievska and Raymond*, 2014; *Raymond et al.*, 2014; *Sessions et al.*, 2015; *Sentić et al.*, 2015].

DCIN is defined as [*Raymond et al.*, 2003]:

$$DCIN = s_T^* - s_S, \tag{3}$$

where s_T^* is the saturated moist entropy averaged from 1750 to 2000 m, and s_S is the moist entropy averaged from 0 to 750 m. Increased DCIN suppresses convection, while low DCIN is conducive to the development of convection. *Sessions et al.* [2016] demonstrated the importance of DCIN in the dry equilibrium, which we will also show in this paper, while *Majda and Khouider* [2001] suggested that convective inhibition is a critical parameter in convective organization.

Moisture and moist entropy are laterally advected from the reference environment by the WTG velocity field. Enforcing WTG creates a vertical velocity, w_{wtg}, which by mass continuity induces lateral transport. NGMS quantifies the large scale transport between the local convection and the environment; it is defined as moist entropy export divided by moisture import [e.g., *Raymond et al.*, 2009]:

$$NGMS = -\frac{T_R S_e}{L_l S_r}, \tag{4}$$

where S_e is the domain average source of entropy laterally imported by the WTG velocity field, S_r is the model source of total water vapor mixing ratio laterally imported by the WTG velocity field, T_R is the reference temperature (300 K in this study), and L_l is the sum of the latent heat of condensation and freezing of water vapor. A number of recent studies have used NGMS as a measure of convective activity in numerical simulations

[*Sobel et al.*, 2014; *Sessions et al.*, 2015, 2016; *Inoue and Back*, 2015a; *Sentić et al.*, 2015], and in observations [*Inoue and Back*, 2015a; *Sentić et al.*, 2015]. Negative NGMS values correspond to situations where both entropy and moisture are exported (or imported), while positive NGMS values correspond to situations where either entropy is imported and moisture is exported, or vice versa. In RCE studies of convective organization, dry regions exhibited negative NGMS, while the intensely convecting regions exhibited positive NGMS [*Bretherton et al.*, 2005].

We also define a characteristic NGMS, $NGMS_c$, which can be defined as the NGMS at the peak precipitation rate [e.g. *Inoue and Back*, 2015a]. $NGMS_c$ is a significant indicator of convective activity [*Inoue and Back*, 2015b; *Sentić et al.*, 2015]; lower $NGMS_c$ is associated with stronger peak precipitation rates because of stronger import of moisture at low NGMS values. Observations from the DYNAMO campaign suggest that the asymptotic NGMS value is around 0.41 for the current climate [*Sentić et al.*, 2015]. An analogous dry characteristic NGMS can be defined for non-precipitating conditions, as the NGMS at lowest DCIN values for a given SST.

2.4. Methodology

In order to generate reference states representative of the large-scale environment, we first run the model in a non-WTG mode for 150 days to a RCE state. We do this for twelve SST values (290, 292, 295, 297, 299, 300, 301, 302, 303, 305, 307, and 310 K), with a shear-free horizontal wind speed of 5 m s^{-1}. The last 30 days of the RCE simulations are averaged to provide the reference temperature and total water vapor mixing ratio profiles for the WTG simulations. For each SST, we perform WTG simulations using RCE profiles with the same SST, by either initializing the domain with the reference

environment moisture profile (moist initialized), or by initializing the domain completely dry (dry initialized). The dry and moist initialized simulations are run for 90 and 45 days, respectively, as in [*Sessions et al.*, 2010], and diagnostic variables are calculated and averaged over the last 30 days of the WTG simulations. Each set of WTG simulations (using a different SST with the corresponding RCE potential temperature and moisture profiles) included horizontal wind speeds ranging from 0 to 20 m s^{-1}.

3. Radiative convective equilibrium

We first characterize the reference environments for all SSTs ranging from 290 K to 310 K, at 5 m s^{-1} horizontal wind speed.

Figures 1a and 1b show profiles of potential temperature and mixing ratio for different SSTs. Higher SSTs produce warmer and moister RCE steady states. Static stability increases, implied by an increase in slope of the potential temperature from the surface to 7 km. The potential temperature and moisture anomalies relative to the 300 K SST are shown in figures 1d and 1e. The potential temperature anomalies increase with SST. The moisture anomaly is greatest at the surface, and it extends deep into the troposphere for high SSTs (up to 14 km), while the dry anomaly, compared to 300 K SST, extends up to about 8 km for lower SSTs.

Figure 2 shows the RCE precipitation rate, saturation fraction, and instability index versus SST. The RCE precipitation rate grows with increasing SSTs from about 3 to about 5 mm d^{-1} (figure 2a) over the range of SSTs used in this study. Since we impose constant insolation, we expect, from the energetics of the problem, a more constant RCE precipitation rate with changing SSTs. However, since we fix greenhouse gas concentrations, we do not account for greenhouse gas effects on radiative cooling which would make

RCE precipitation rates constant with SST. Consequently, in our simulations we decouple convective warming of the atmosphere, from warming due to greenhouse gas effects. We find this study to be a useful exercise in understanding how convection changes with SST, despite the fact that it cannot be directly associated with the real climate system. We leave the study of effects of greenhouse gases on convective organization in the context of WTG simulations for future studies.

The RCE saturation fraction, which is a measure of moisture content, grows from 0.73 at cool SSTs to 0.85 at high SSTs (figure 2b). Note that a small increase in saturation fraction corresponds to a large increase in water vapor content in the troposphere (compare to figure 1b). The RCE atmospheric instability index increases from about 2 J K^{-1} kg^{-1} at 290 K SST, to about 26 J K^{-1} kg^{-1} at 310 K SST (figure 2f); increase in instability index with SST suggests a more unstable atmosphere to moist convection.

In the next section we study how local convection responds to changes in the RCE reference environment presented in this section. Specifically, we will analyze the non-precipitating and precipitating equilibrium states in light of organized convection and dry regions that surround it.

4. Multiple equilibria in precipitation

Multiple equilibria in precipitation are defined as having both precipitating and non-precipitating steady states for a given reference environment (potential temperature and mixing ratio profiles), and surface conditions (i.e. SST and imposed wind speed), depending on whether the model is initialized dry or moist [*Sobel et al.*, 2007; *Sessions et al.*, 2010]. Figure 3 shows the precipitation rate versus horizontal wind speed for SSTs of 290, 300, 303, and 310 K, for simulations that are either initialized dry (dotted lines with open

symbols) or moist (solid lines with solid symbols). Multiple equilibirum experiments for a given SST use the reference RCE environment at the same SST (e.g. simulations shown in figure 3 having SST of 310 K were performed with reference profiles of 310 K SST RCE simulation). Regions of multiple equilibria are defined as the range of wind speeds supporting both a dry and a precipitating state (e.g., 3 to 12 m s^{-1} for 303 K SST). We notice that:

1. Higher SSTs support larger precipitation rates compared to lower SSTs.

2. The range of wind speeds that support multiple equilibria in precipitation differs for different SSTs. For example, it is 7 to 16 m s^{-1} for 290 K SST, and only from 0 to 6 m s^{-1} for 310 K SST.

3. The range of wind speeds that support a single non-precipitating state also varies with SSTs. It is 0 to 7 m s^{-1} for 290 K SST and does not exist for 310 K SST.

4. The wind speed where multiple equilibria transition to a single equilibrium, which we define as the critical wind speed, varies with SST.

We can generalize these results to all SSTs by considering a phase diagram that distinguishes multiple from single equilibria. Figure 4 shows a phase diagram of precipitation as a function of horizontal wind speed and SSTs; dry initialized simulations are shown in figure 4a, while figure 4b shows the corresponding diagram for moist initialized simulations. Solid symbols represent precipitating, while empty symbols represent non-precipitating steady states.

Figure 4 also shows two curves: the solid and dashed curves present eye guides for the SST dependence of the critical wind speeds separating multiple equilibria from the

single precipitating equilibrium, and multiple equilibria from the single non-precipitating equilibrium, respectively. These curves separate three regions:

1. A region of high wind speeds across all SSTs where a single precipitating equilibrium exists; we interpret this as conditions favoring less organized convection.

2. A region of intermediate wind speeds across all SSTs where multiple equilibria exist; we interpret this as a region of conditions favoring organized convection; under these conditions there exists the possibility for organized convective regions to be surrounded by dry non-precipitating regions.

3. A region of low wind speeds and low SSTs where a single non-precipitating equilibrium exists, where convection cannot form even in a moist environment.

The region of organized convection (second point in the list above) where multiple equilibria exist shows an interesting pattern with changing SSTs. At low SSTs, the region is narrow compared to the median 300 K SST, and exists for higher wind speeds. At high SSTs, this region is narrow but exists for low wind speeds. This pattern is reasonable in light of warmer and moister reference profiles at higher SSTs; the reference environment permits precipitation to occur at lower surface moist entropy forcing. However, the largest range of wind speeds supporting organized convection exists around 300 K SST, which is closer to the current SST values in the tropics. This suggests that convective organization occurs more readily at low wind speeds for higher SSTs, while any increase in surface fluxes beyond this region results in more widespread, less organized, convection. Note, however, that changing model parameters might influence the shape of these boundaries. Also, the WTG approximation by design does not take into account dynamical organizing effects such as cold pools [e.g. *Coppin and Bony*, 2015] which might induce convective

organization even in the region of low SSTs and wind speeds which do not support a precipitating equilibrium.

Examining the transition from multiple to a single precipitating equilibrium can inform us about mechanisms that affect the critical wind speed and range of multiple equilibria, and, consequently, convective organization. In the next section, we diagnose this transition for the 300 K SST.

5. Diagnosing convection and multiple equilibria at the 300 K SST

In this section we diagnose the transition from the multiple-to-single precipitating equilibrium, and discuss the conditions supporting the single non-precipitating equilibrium; the precipitation rate, saturation fraction, instability index, DCIN, and NGMS, are useful diagnostics for characterizing this transition. Also, we diagnose the precipitating equilibrium. We do this for the 300 K SST; other SSTs show qualitatively similar behavior. We discuss the non-precipitating and precipitating simulations with changing SSTs in the subsequent sections.

Figure 5 shows the precipitation rate, saturation fraction, and instability index, for the moist (solid lines and symbols) and the dry (dashed lines and empty symbols) initialized simulations, with the RCE values shown with a dash-dotted line, for comparison. To explain the changes in these diagnostics, we examine DCIN and NGMS in figure 6; figure 6 also shows the components of DCIN (s_T^* and s_T in equation 3; figures 6c and 6e) and NGMS (S_e and S_r, entropy export and moisture import in equation 4; figures 6d and 6f).

The dry initialized non-precipitating simulations show a steady increase in saturation fraction with wind speed until 15 m s^{-1} when there is a jump to higher saturation fraction values (figure 5b), lower instability index (figure 5c), and lower DCIN (figure 6a).

Low-wind-speed dry-initialized simulations are extremely dry compared to saturated conditions which can be seen in the boundary layer moist entropy s_S component of DCIN (figure 6e). Note that the change in DCIN arises from changes in s_S (figure 6b), rather than from the changes in s_T^* (figure 6c) which depends only on temperature for a given pressure level. A small increase in horizontal wind speed from 16 to 17 m s^{-1} increases the surface moist entropy enough for parcels to overcome DCIN, which leads to conditions supporting convection. Also, the non-precipitating simulations have saturation fractions much lower than the RCE (figure 5b, dash dotted line), and instability index values close to the RCE (figure 5c, dash dotted line); the former is observed in dry regions of organized convection in other studies [e.g. *Bretherton et al.*, 2005]. The non-precipitating simulations are also characterized by an increase in moist entropy export (figure 6d) and moisture export (figure 6f, negative import) with increasing wind speed, which results in a decreasing negative NGMS with increased wind speed (figure 6b). This is in agreement with previous studies of organized convection [*Bretherton et al.*, 2005; *Muller and Held*, 2012; *Wing and Emanuel*, 2013], where dry regions are characterized by negative NGMS. After the transition to a precipitating steady state, the dry initialized simulations show little difference from the moist initialized precipitating simulations.

Steady state vertical profiles of WTG mass flux, radiation, and entropy (dry, moist and saturated), shown in figure 7, can help us understand the moistening in the non-precipitating simulations. Figures 7a–c show these diagnostics for the 2 m s^{-1} wind speed. Strong cooling at the top of the boundary layer (figure 7b) produces a WTG mass flux with descent throughout the troposphere and into the boundary layer (figure 7a), with a maximum at the top of the boundary layer. This is correlated with drying seen

in the moist entropy profile (figure 7c). Even the moist initialized simulation loses most of its initial moisture, going from 0.8 RCE value to 0.3 saturation fraction (figure 5b). At 15 m s^{-1}, which is around the critical wind speed (transition from the multiple to the single precipitating equilibrium), the non-precipitating simulation develops a circulation (figure 7d), with an upward mass flux in the boundary layer. This circulation raises the boundary layer height (which can be diagnosed via the increase in radiative cooling maximum shown in figure 7e), and increases the moist entropy in and above the boundary layer (figure 7f), and consequently the saturation fraction (figure 5b). A small increase in wind speed beyond the critical wind speed causes sufficient moistening to decrease the DCIN enough to tip the dry initialized simulations into a precipitating state. The precipitating simulations at 15 m s^{-1}, and 20 m s^{-1} (red curve in figures 7d–f, and all curves in figures 7g–i), show qualitatively similar behavior. There is a strong positive vertical mass flux (figures 7d and 7g), a more uniform cooling with height (figures 7e and 7h), and a very moist moist entropy profile (figures 7f and 7i).

The simulations at 2 m s^{-1} are of particular interest because they belong to the region of SSTs and wind speeds which support a single non-precipitating equilibrium. The moist initialized simulation has the same saturation fraction (figure 5b) and s_S (figure 6e) as the dry initialized simulation, despite being initialized with a moist reference profile. This is a consequence of a balance between radiative cooling which causes downward mass flux (figures 7b and 7a, respectively), export of moist entropy due to WTG circulations, and surface entropy flux forcing, resulting in net drying from initially moist conditions. We find that the downward mass flux, entropy export, and drying exists in all the simulations in the region of SSTs and wind speeds at which there is the single non-precipitating

equilibrium. Also, those simulations show positive NGMS (figure 6b), going to small or negative values near the single non-precipitating to multiple equilibria transition. We will further address this NGMS behavior in section 6.

Precipitating simulations show an increase in precipitation rate (figure 5a) and saturation fraction (figure 5b), and a decrease in instability index (figure 5c) with increasing wind speed. To understand this, we consider the essence of the WTG approximation. In precipitating simulations, a convective event in the model produces a warming anomaly (positive in the middle troposphere, negative near the surface due to evaporative cooling of rain, not shown) which causes a reduction in the instability index (figure 5c). The lower instability index is associated with a change in the mass flux via changes in the vertical WTG velocity (equation 1) which is generated to offset the heating anomaly. The vertical mass flux modulates the import of moisture (figure 6f) which in turn affects the saturation fraction. It is straightforward to show (see appendix) that:

$$P = \int_0^h \rho(S_r + S_{rs})dz, \tag{5}$$

where ρ is the density, P the precipitation rate, S_r the lateral transport of moisture due to the WTG vertical velocity field (from equation 4), S_{rs} is the total water vapor mixing ratio source due to surface fluxes, h is the tropopause height (15 km in this study), and z is the height. In the appendix we show that the WTG transport term models the bulk of the precipitation rate accurately, especially at high wind speeds. The increase in precipitation rate with wind speed is caused by stronger potential temperature perturbations which strengthen the WTG mass flux which causes a stronger import of moisture and thus higher precipitation rates. These high precipitation rates, and high saturation fractions,

are observed in precipitating regions of self-aggregation simulations [e.g. *Bretherton et al.*, 2005].

6. Diagnosing convection at different SSTs

Relationships between convective diagnostics are a convenient way of summarizing the results from the previous section. They can also be used to show how organized convection, specifically the dry, non-precipitating, regions, and the moist, precipitating, regions, behave as as function of SST. First, we look at vertical profiles of the WTG simulations for a single wind speed, but different SSTs, to diagnose general characteristics of WTG simulations at different SSTs. Second, we focus on diagnostic relationships for precipitating simulations; the precipitating state gives information about the nature of convection for different SSTs. Then we focus on diagnostics and relationships relevant for non-precipitating simulations and we discuss boundary layer influences which maintain the dry state.

6.1. Vertical profiles at different SSTs

Figure 8 shows vertical profiles of radiative cooling and WTG mass flux, for dry and moist initialized simulations at 5 m s^{-1} wind speed, for different SSTs. We find strong radiative cooling at the top of the boundary layer for all of the dry initialized non-precipitating simulations (figure 8a). Higher SSTs also exhibit stronger cooling above and decreased cooling below about 4 km, compared to lower SSTs. The vertical mass flux profiles show weakening with increased SST (figure 8c) for dry initialized non-precipitating simulations, both in and above the boundary layer. Moist initialized simulations remain non-precipitating only for SSTs of 290 and 295 K, in which case they resemble the steady

state of dry initialized simulations. Precipitating simulations, however, show a uniform radiative cooling profile throughout the troposphere with with radiative warming at the surface for higher SSTs (figure 8b), and an increase in mass flux (figure 8d) with SST. The simulation at 300 K SST is more uncertain because it is right on the boundary of the single non-precipitating to multiple equilibria transition; in that simulation convection becomes intermittent with quiet and precipitating periods which average to less well defined mass flux profile. These vertical profiles will help us to explain some results below.

6.2. Precipitating simulations

An example of an important diagnostic relationship relates precipitation rate to column moisture content [*Raymond et al.*, 2003; *Bretherton et al.*, 2004; *Peters and Neelin*, 2006; *Raymond et al.*, 2007; *Neelin et al.*, 2009; *Sherwood et al.*, 2010; *Masunaga*, 2012; *Sessions et al.*, 2015; *Sentić et al.*, 2015]. *Sherwood et al.* [2010] found that general circulation models improved when precipitation was a function of moisture. Other studies found a strong connection between precipitation rate and atmospheric stability [*Raymond and Sessions*, 2007; *Gjorgjievska and Raymond*, 2014; *Inoue and Back*, 2015a; *Sentić et al.*, 2015], between large-scale transport and precipitation rate, atmospheric stability, and column moisture content [*Inoue and Back*, 2015a; *Sessions et al.*, 2015; *Sentić et al.*, 2015], and between saturation fraction and instability index [*Gjorgjievska and Raymond*, 2014; *Sessions et al.*, 2015; *Sentić et al.*, 2015]. Figure 9 shows the precipitation rate as a function of saturation fraction, instability index, and NGMS; and saturation fraction versus instability index. They include only precipitating steady states independent of initial moisture. The simulations at 300 K SST, which we studied in the previous section, are shown in black.

The relationship between precipitation rate and saturation fraction shows a well substantiated finding; higher saturation fraction leads to higher precipitation rates [*Bretherton et al.*, 2004; *Peters and Neelin*, 2006; *Masunaga*, 2012; *Gjorgjievska and Raymond*, 2014; *Sentić et al.*, 2015]; for comparison, the relationship from *Bretherton et al.* [2004] is shown in figure 9a with a black dashed line. Compared to the 300 K SST, higher SSTs support higher saturation fractions, which in turn support higher precipitation rates; the maximum precipitation rate at 310 K SST is more than double the 300 K maximum value. These results suggest that the SSTs set the characteristic asymptotic value of precipitation rate by shifting saturation fraction to higher (or lower) values compared to the 300 K SST.

The precipitation rate-instability index inverse relationship [*Sessions et al.*, 2010; *Gjorgjievska and Raymond*, 2014; *Sessions et al.*, 2015; *Sentić et al.*, 2015; *Sessions et al.*, 2016; *Raymond and Flores*, 2016a] strengthens with increasing SSTs (figure 9b); a lower instability index is associated with stronger precipitation rates for a given SST. Furthermore, for a given SST a lower instability index is associated with stronger surface winds which strengthen convection, via stronger mass flux (not shown), and the lateral import of moisture (figure 6a) which increases the saturation fraction (figure 5b) and, consequently, the precipitation rate (figure 5a). This relationship was also found in the DYNAMO field campaign observations [*Sentić et al.*, 2015], and discussed in *Raymond and Flores* [2016b]. It is important to note that changes in instability index can occur in different ways which we do not explore in this paper. For example, *Sentić et al.* [2015] show that a lower instability index can occur even for non-precipitating conditions in DYNAMO observations,

which suggests that the WTG approximation does not include all the mechanism which can affect the instability index.

NGMS characterizes the response of convection to environmental forcing. A low, positive NGMS is associated with stronger import of moisture and export of moist entropy. In our WTG simulations, the NGMS asymptotes to a characteristic value, $NGMS_c$, in steady state, for high wind speeds (figures 9c); this behavior was found in other WTG studies [*Sessions et al.*, 2010]. $NGMS_c$ decreases from about 0.5 at 290 K SST, to about 0.2 at 310K SST. Observations from the DYNAMO campaign suggest that the asymptotic NGMS value is around 0.41 for the current climate [*Sentić et al.*, 2015]; this value is overlaid in figure 9c for comparison. Note that the modeled and DYNAMO observed value of $NGMS_c$ differs significantly; *Sentić et al.* [2015] suggest possible reasons for the discrepancy (of which the microphysics parameterization might be the most important one).

The relationship between saturation fraction and instability index is shown in figure 9d; a low instability index correlates with a higher saturation fraction. The inverse relationship between saturation fraction and instability index is preserved for different SSTs, but also depends strongly on the SST. At high SSTs, the same decrease in instability index is associated with a smaller increase in saturation fraction than at lower SSTs. Although the increment in saturation fraction is relatively small for high SSTs, it is not insignificant; at high SSTs the precipitation is more sensitive to small changes in saturation fraction than at low SSTs (figure 9a). Also, moderate SSTs (300, 303 and 307 K SSTs) support a wider range of the instability index values compared to high and low SSTs (figure 9d). Furthermore, changes in saturation fraction are strongly correlated with changes in the

instability index; a lower instability index strengthens the WTG mass flux (figure 8d) in the lower, moister, troposphere, which is associated with an increase in moisture import (not shown). This behavior was observed in DYNAMO [*Sentić et al.*, 2015]; the fit to the observed saturation fraction–instability index relationship from DYNAMO is plotted in figure 9d for comparison.

In conclusion, the changes in diagnostics influenced by different SSTs, summarized via diagnostic relationships, show how precipitating regions in organized convection might change with changing SSTs. Higher SSTs support higher saturation fractions, but the saturation fraction is less sensitive to changes in atmospheric stability (figure 9d). On the other hand, the precipitation rate is more sensitive to small changes in saturation fraction and instability index at high SSTs (figure 9a and figure 9b). The change in the characteristic NGMS value signifies strengthening of convection; lower $NGMS_c$ quantifies the decrease in the ratio between entropy export and moisture import. Small and positive NGMS is associated with more intense precipitation [*Raymond et al.*, 2009; *Inoue and Back*, 2015a; *Sentić et al.*, 2015], which implies that with increasing SSTs, convection in precipitating regions of organized convection might get stronger. Furthermore, a lower instability index is associated with higher saturation fractions and precipitation rates [*Gjorgjievska and Raymond*, 2014; *Sessions et al.*, 2015; *Sentić et al.*, 2015]. Our results suggest that with increasing SSTs, the relationship between saturation fraction and precipitation rate might get stronger due to lower instability indices. Changes in the instability index are directly related to temperature anomalies which arise from local domain warming anomalies. We found that changing SSTs influence changes in the warm-

ing anomaly, which influences the instability index and WTG mass flux, and consequently moisture import and precipitation rate changes (see appendix).

Next, we investigate non-precipitating simulations to assess how dry regions in organized convection change with changing SSTs.

6.3. Non-precipitating simulations

In the previous section we discussed how the convection changes with SST in WTG multiple equilibria simulations. However, convective organization is also characterized by the existence of strong subsidence regions; *Sessions et al.* [2016] pointed out the importance of DCIN in modelling dry regions of convective organization. Here we diagnose the non-precipitating simulations to better understand the transition from multiple equilibria to the single precipitating equilibrium, and to assess how dry regions change with SST.

Figure 10 shows DCIN versus saturation fraction; mean moist entropy averaged in a layer between 0 and 1750 m (s_S), versus surface entropy flux; surface entropy flux versus the horizontal wind speed; and NGMS versus DCIN, for different SSTs for non-precipitating simulations. The simulations at 300 K SST, which we studied in the previous section, are shown in black. In figure 11, we also show the wind speed variations of DCIN and its components, the threshold saturated moist entropy, s_T^*, and boundary layer moist entropy, s_S; and wind speed variations of NGMS and its components, the WTG lateral entropy export, and the WTG lateral mixing ratio import, for different SSTs. In these simulations we focus only on the simulations below the dashed line in figure 4; we also exclude the non-precipitating simulation at 20 m s^{-1} for 290 K SST, which does not affect our conclusions.

Sessions et al. [2016] showed that non-precipitating WTG simulations are characterized by high values of DCIN. *Majda and Khouider* [2001] suggested convective inhibition (of which DCIN is a related measure) as a critical parameter for diagnosing convective organization. In section 5, we found DCIN to be important in maintaining the dry state prior to the transition to a single precipitating equilibrium. Figure 10a shows that a decrease in DCIN is associated with increased moisture content at a given SST; there is a linear relationship between DCIN and saturation fraction, which increases slope for increasing SSTs. This suggests that for the same incremental increase in wind speed, DCIN decreases more for higher SSTs than for lower SSTs. The decrease in DCIN might help identify the mechanism which permits higher SSTs to exhibit lower critical wind speeds for the multiple-to-single precipitating equilibrium transition. Specifically, this might be a direct consequence of changes in the thermodynamics at different SSTs; the mean moist entropy from 0 to 1750 m (s_S, figure 10b) increases with surface entropy fluxes, which in turn increase with increasing wind speeds (figure 10c). Surface entropy fluxes, on the other hand, are directly influenced by the SST; for the same wind speed, higher SSTs support stronger surface entropy fluxes (figure 10c). The changes in DCIN (figure 11a) are associated primarily with increases in the surface moist entropy (compare figure 10b, figure 11c, and figure 11e); the threshold saturated entropy, s_T^*, remains constant with wind speed for each SST (figure 11c). Furthermore, the NGMS decreases to negative values with decreasing DCIN (figure 10d). The dry characteristic NGMS value at which the simulations show a minimum in DCIN for the respective SST is similar for 290, 295 and 300 K; it is about -0.4. Above 300 K, however, it increases to higher values (about -0.2 at 310 K SST). This behavior suggests that the NGMS export of entropy and moisture in

the non-precipitating simulations might influence the critical wind speed for the transition from multiple to a single precipitating equilibrium (dashed line in figure 4). We also note that moisture export increases with wind speed and SST (figure 11f), despite the decrease in mass flux with SST (figure 8c). The troposphere is moister over oceans with higher SSTs, thus any descending motion (even if weaker, figure8c) can export more moisture. Higher wind speeds also supply more moisture for export, thus strengthening the overall up-gradient transport of moisture at higher SSTs.

Previous research demonstrated up-gradient horizontal transport of moisture (transport of moisture from dry to moist regions) in organized convection, which is characterized by negative NGMS [*Bretherton et al.*, 2005; *Muller and Held*, 2012; *Wing and Emanuel*, 2013]. In our non-precipitating simulations, the NGMS is mostly negative (figures 10d, and 11b); a negative NGMS is characterized by export of both entropy and moisture. Most of the simulations with positive NGMS correspond to the region of the single non-precipitating equilibrium (below the solid line in figure 4). They exhibit a positive NGMS because of the moist entropy import for lowest imposed wind speeds (figure 11d). Other simulations show a decrease of NGMS with an increase in wind speed (figure 11b), because both the moist entropy and moisture are exported (figures 11d, and 11f). Moisture export (figure 11f) is directly related to changes in surface entropy forcing (figure 10c): the more surface evaporation, the more moisture is exported up to boundary layer saturation, at which point, surface fluxes exceed what can be physically transported laterally and the moisture penetrates the top of the boundary layer, resulting in a precipitating state.

The diagnostics in the non-precipitating simulations show the importance of DCIN for diagnosing the transition from the multiple to the single precipitating equilibrium.

Higher SSTs support more moistening for the same increment in wind speed compared to low SSTs. This is associated with a stronger decrease in DCIN at higher SSTs for lower wind speeds compared to low SSTs. Furthermore, a stronger export of entropy and moisture with wind speed lowers the NGMS into negative values, which is analogous to strengthening the up-gradient transport of moisture from the dry regions to moist regions in organized convection.

7. Summary and conclusions

In this study, we performed weak temperature gradient (WTG) simulations of multiple equilibria in precipitation at different SSTs in order to study how diagnostics in dry and precipitating regions of convective organization might change with changing SSTs. At different SSTs, we used RCE temperature and total water vapor mixing ratio profiles as reference profiles for the WTG simulations, which, depending on if the WTG domain was initialized dry or moist, exhibited a dry or precipitating steady state. We assumed the hypothesized analogy between precipitating and non-precipitating WTG equilibria, and the precipitating and dry regions in organized convection. We found three regions in the SST versus wind speed phase space (figure 4):

1. A region with high wind speeds and a single precipitating equilibrium, which can be interpreted as the region of less organized, scattered, convection (above the dashed line in figures 4a–b), characteristic of a disorganized state.

2. A region with intermediate wind speeds which support both a non-precipitating and a precipitating steady state (between the dashed and solid line in figures 4a–b), i.e. multiple equilibria, which can be interpreted as conditions supporting convective organization.

606 3. A region with low wind speeds and SSTs, which does not support convection even
607 in a moist environment (below solid line in figures 4a–b).

608 The transition from the non-precipitating equilibrium to a precipitating equilibrium is
609 accompanied by an increased saturation fraction due to a boundary layer circulation which
610 moistens the lower troposphere and leads to lower DCIN which supports the development
611 of convection. This boundary layer circulation strengthens with increasing wind speeds
612 and opposes radiatively driven subsidence.

613 We studied how multiple equilibria change with SSTs, and found that the range of
614 wind speeds supporting multiple equilibria is the largest around 300 K SST and becomes
615 smaller for lower and higher SSTs. Also, the wind speeds supporting multiple equilibria are
616 smaller at high SSTs than at low SSTs, suggesting that at high SSTs organized convection
617 might occur more readily for lower surface forcing. We also diagnosed convection for
618 different SSTs and surface wind speeds. Diagnostic relationships significant for convective
619 organization suggest:

620 1. Higher SSTs support higher saturation fractions (as well as total water vapor mixing
621 ratios), which in turn support higher precipitation rates.

622 2. A stronger relationship exists between instability index and precipitation rate, and
623 saturation fraction and instability index for higher SSTs. The precipitating WTG simu-
624 lations show a more pronounced decrease in instability index with wind speed for higher
625 SSTs. Previous WTG studies showed that decreasing instability index concentrates mois-
626 ture convergence at low levels which increases saturation fraction, and consequently the
627 precipitation rate.

628 3. Differences in the large-scale transport between non-precipitating and precipitating
629 simulations also increase with SST. The characteristic NGMS value, which quantifies
630 the strength of large-scale circulations, decreases with SST for precipitating simulations.
631 The analogous dry characteristic NGMS, on the other hand, increases with SST for non-
632 precipitating simulations. This suggests strengthening of the up-gradient transport of
633 moisture from dry to precipitating regions of organized convection for high SSTs.

634 In conclusion, our results suggest that the precipitating and the non-precipitating WTG
635 multiple equilibria simulations show significant strengthening of organized convection with
636 increasing SSTs, via increased precipitation rates, moistening, lower atmospheric stability,
637 and enhanced up-gradient transport of moisture from the dry regions to the precipitating
638 regions. The limitations of this study, in application to the real atmosphere, are the ideal-
639 ized set of parameters used, and fixing of the greenhouse gas concentration. Nonetheless,
640 this study identifies important processes and diagnostic relationships to consider in future
641 modeling and observational studies of convective organization.

Appendix A: Modeling WTG precipitation rates

To model WTG precipitation rates, we start with the total water vapor mixing ratio tendency equation [r_t, e.g. *Herman and Raymond*, 2014]:

$$\frac{\partial \rho r_t}{\partial t} + \nabla \cdot (\rho \mathbf{v} r_t - K \nabla r_t) = \rho (S_{rs} + S_{rp} - S_r), \tag{A1}$$

where ρ is the density, K is the eddy-mixing coefficient, $\mathbf{v}$ is the velocity vector, S_{rs} is the total water vapor mixing ratio source due to surface fluxes, S_{rp} is minus the conversion rate of cloud water to precipitation, and S_r the source of total water vapor mixing ratio due to WTG transport [for a complete form of the WTG transport please see *Herman and*

Raymond, 2014]. Assuming a steady state, and neglecting advection (assuming that WTG advection is more important in transporting moisture) , we can integrate equation A1 from the surface to the tropopause to get:

$$P = \int_0^h \rho \left(S_r - S_{rs} \right) dz, \tag{A2}$$

where we define the precipitation rate as $P = \int_0^h \rho S_{rp} dz$.

Figure 12 shows the precipitation rate versus wind speed at 300 K SST, and precipitation rate versus SST for a wind speed of 10 m s^{-1}, for the WTG model, the simple model from equation A2, and the simple model from equation A2 excluding the surface flux term (S_{rs}). The wind speed dependence (figure 12a) shows that the simple model reproduces the WTG precipitation rate. However, excluding the surface fluxes (dashed red line in figure 12a) shows that the bulk of the precipitation comes from the WTG mixing ratio transport, via mass continuity driven by the WTG mass flux. Similar results hold for the SST dependence (figure 12b). These result show that the WTG precipitation rate is dominated by the WTG mass transport, especially at high wind speeds and SSTs.

Acknowledgments.

We thank David Raymond, Michael Herman, Patrick Haertel, and Larissa Back for fruitful discussions. We also thank 3 anonymous reviewers whose comments improved the focus of this manuscript. We would like to thank NCARs Advanced Study Program for support during part of the writing of this manuscript. We would like to acknowledge high-performance computing support from Yellowstone (ark:/85065/d7wd3xhc) provided by NCAR's Computational and Information Systems Laboratory, sponsored by the National Science Foundation. The model data used in this study can be obtained by contacting the corresponding author (stipo.sentic@student.nmt.edu). This work was supported by

U.S. National Science Foundation Grants AGS-1056254, ATM-1021049, AGS-1342001, and AGS-1561084.

References

Abbot, D. S. (2014), Resolved snowball earth clouds, *J. Climate*, *27*(12), 4391–4402, doi:10.1175/JCLI-D-13-00738.1.

Anber, U., S. Wang, and A. Sobel (2014), Response of atmospheric convection to vertical wind shear: Cloud-system-resolving simulations with parameterized large-scale circulation. Part I: Specified radiative cooling, *J. Atmos. Sci.*, *71*, 2976–2993, doi:10.1175/JAS-D-13-0320.1.

Anber, U., S. Wang, and A. Sobel (2015), Effect of surface fluxes versus radiative cooling on tropical deep convection, *J. Atmos. Sci.*, *72*, 3378–3388, doi:10.1175/JAS-D-14-0253.1.

Beucler, T., and T. W. Cronin (2016), Moisture-radiative cooling instability, *J. Adv. Model. Earth Sys.*, *8*(4), 1620–1640, doi:10.1002/2016MS000763.

Bretherton, C. S., and P. K. Smolarkiewicz (1989), Gravity waves, compensating subsidence and detrainment around cumulus clouds, *J. Atmos. Sci.*, *46*, 740–759.

Bretherton, C. S., M. E. Peters, and L. E. Back (2004), Relationships between water vapor path and precipitation over the tropical oceans, *J. Climate*, *17*(7), 1517–1528.

Bretherton, C. S., P. N. Blossey, and M. Khairoutdivnov (2005), An energy-balance analysis of deep convective self-aggregation above uniform SST, *J. Atmos. Sci.*, *62*, 4273–4292, doi:10.1175/JAS3614.1.

Coppin, D., and S. Bony (2015), Physical mechanisms controlling the initiation of convective self-aggregation in a general circulation model, *J. Adv. Model. Earth Syst.*, *7*(4), 2060–2078.

Daleu, C. L., e. a. (2016), Intercomparison of methods of coupling between convection and large-scale circulation: I. comparison over nonuniform surface, *J. Adv. Model. Earth Syst.*, *8*, 387–405, doi:doi:10.1002/2015MS000570.

Emanuel, K., A. A. Wing, and E. M. Vincent (2014), Radiative-convective instability, *J. Adv. Model. Earth Syst.*, *6*(1), 75–90.

Gjorgjievska, S., and D. J. Raymond (2014), Interaction between dynamics and thermodynamics during tropical cyclogenesis, *Atmos. Chem. Phys.*, *14*, 3065–3082, doi:10.5194/acp-14-3065-2014.

Herman, M. J., and D. J. Raymond (2014), WTG cloud modeling with spectral decomposition of heating, *J. Adv. Model. Earth Syst.*, *6*, 1121–1140, doi:10.1002/2014MS000359.

Holloway, C. E., and S. J. Woolnough (2016), The sensitivity of convective aggregation to diabatic processes in idealized radiative-convective equilibrium simulations, *J. Adv. Model. Earth Sys.*, *8*(1), 166–195, doi:10.1002/2015MS000511.

Inoue, K., and L. Back (2015a), Gross moist stability assessment during TOGA COARE: Various interpretations of gross moist stability, *J. Atmos. Sci.*, *72*(11), 4148–4166, doi:10.1175/JAS-D-15-0092.1.

Inoue, K., and L. Back (2015b), Column-integrated moist static energy budget analysis on various time scales during TOGA-COARE, *J. Atmos. Sci.*, *72*(5), 1856–1871, doi:10.1175/JAS-D-14-0249.1.

Majda, A. J., and B. Khouider (2001), Stochastic and mesoscopic models for tropical convection, *Proc. Natl. Acad. Sci.*, *99*, 1123–1128.

Masunaga, H. (2012), Short-term versus climatological relationship between precipitation and tropospheric humidity, *J. Climate*, *25*, 7983–7990, doi:10.1175/JCLI-D-12-00037.1.

Mlawer, E., S. Taubman, P. Brown, M. Iacono, and S. Clough (1997), RRTM, a validated correlated-k model for the longwave, *J. Geophys. Res.*, *102*(16), 663–682.

Muller, C. J., and I. M. Held (2012), Detailed investigation of the self-aggregation of convection in cloud-resolving simulations, *J. Atmos. Sci.*, *69*, 2551–2565, doi:10.1175/JAS-D-11-0257.1.

Neelin, J. D., O. Peters, and K. Hales (2009), The transition to strong convection, *J. Atmos. Sci.*, *66*(8), 2367–2384.

Peters, O., and J. D. Neelin (2006), Critical phenomena in atmospheric precipitation, *Nat. Phys.*, *2*, 393–396, doi:10.1038/nphys314.

Raymond, D. J. (2001), A new model of the madden-julian oscillation, *J. Atmos. Sci.*, *58*(18), 2807–2819, doi:10.1175/1520-0469(2001)058<2807:ANMOTM>2.0.CO;2.

Raymond, D. J. (2007), Thermodynamic control of tropical rainfall, *Q. J. Roy. Meteor. Soc.*, *126*(564), 889–898, doi:10.1002/qj.49712656406.

Raymond, D. J., and M. M. Flores (2016a), Predicting convective rainfall over tropical oceans from environmental conditions, *J. Adv. Model. Earth Syst.*, *8*, 703–718, doi:10.1002/2015MS000595.

Raymond, D. J., and M. M. Flores (2016b), Predicting convective rainfall over tropical oceans from environmental conditions, *J. Adv. Model. Earth Syst.*, *8*, 703–718, doi:doi:10.1002/2015MS000595.

Raymond, D. J., and S. L. Sessions (2007), Evolution of convection during tropical cyclogenesis, *Geophys. Res. Lett.*, *34*, L06,811, doi:10.1029/2006GL028607.

Raymond, D. J., and X. Zeng (2005), Modelling tropical atmospheric convection in the context of the weak temperature gradient approximation, *Q. J. Roy. Meteor. Soc.*, *131*, 1301–1320, doi:10.1256/qj.03.97.

Raymond, D. J., G. B. Raga, C. S. Bretherton, J. Molinari, C. López-Carrillo, and Ž. Fuchs (2003), Convective forcing in the intertropical convergence zone of the Eeastern Pacific, *J. Atmos. Sci.*, *60*, 2064–2082.

Raymond, D. J., S. L. Sessions, and Z. Fuchs (2007), A theory for the spinup of tropical depressions, *Q. J. Roy. Meteor. Soc.*, *133*, 1743–1754, doi:10.1002/qj.125.

Raymond, D. J., S. L. Sessions, A. H. Sobel, and Z. Fuchs (2009), The mechanics of gross moist stability, *J. Adv. Model. Earth Syst.*, *1*(3), 9, doi:10.3894/JAMES.2009.1.9.

Raymond, D. J., S. Gjorgjievska, S. L. Sessions, and Z. Fuchs (2014), Tropical cyclogenesis and mid-level vorticity, *Austral. Meteor. Ocean. J.*, *64*, 11–25.

Schreck III, C. J. (2015), Kelvin waves and tropical cyclogenesis: A global survey, *Month. Weath. Rev.*, *143*(10), 3996–4011.

Sentic, S., S. L. Sessions, and Željka Fuchs (2015), Diagnosing DYNAMO convection with weak temperature gradient simulations, *J. Adv. Model. Earth Syst.*, doi:10.1002/2015MS000531.

Sessions, S. L., S. Sugaya, D. J. Raymond, and A. H. Sobel (2010), Multiple equilibria in a cloud resolving model using the weak temperature gradient approximation, *J. Geophys. Res.*, *115*(D12), D12110, doi:10.1029/2009JD013376.

748 Sessions, S. L., M. J. Herman, and S. Sentic (2015), Convective response to changes in
749 the thermodynamic environment in idealized weak temperature gradient simulations,
750 *J. Adv. Model. Earth Sys.*, *7*, 712–738, doi:10.1002/2015MS000446.

751 Sessions, S. L., S. Sentic, and M. J. Herman (2016), The role of radiation in organizing
752 convection in weak temperature gradient simulations, *J. Adv. Model. Earth Syst.*, doi:
753 10.1002/2015MS000587.

754 Sherwood, S. C., R. Roca, T. M. Weckwerth, and N. G. Andronova (2010), Tropospheric
755 water vapor, convection, and climate, *Rev. Geophys.*, *48*(2), doi:10.1029/2009rg000301.

756 Singh, M. S., and P. A. O'Gorman (2013), Influence of entrainment on the thermal strat-
757 ification in simulations of radiative-convective equilibrium, *Geophys. Res. Let.*, *40*(16),
758 4398–4403, doi:10.1002/grl.50796.

759 Singh, M. S., and P. A. O'Gorman (2015), Increases in moist-convective updraught ve-
760 locities with warming in radiative-convective equilibrium, *Q. J. Roy. Meteor. Soc.*,
761 *141*(692), 2828–2838, doi:10.1002/qj.2567.

762 Singh, M. S., and P. A. O'Gorman (2016), Scaling of the entropy budget with surface
763 temperature in radiative-convective equilibrium, *Journal of Advances in Modeling Earth*
764 *Systems*, pp. n/a–n/a, doi:10.1002/2016MS000673.

765 Sobel, A., S. Wang, and D. Kim (2014), Moist static energy budget of the MJO during
766 DYNAMO, *J. Atmos. Sci.*, *71*(11), 4276–4291, doi:10.1175/JAS-D-14-0052.1.

767 Sobel, A. H., and C. S. Bretherton (2000), Modeling tropical precipita-
768 tion in a single column, *J. Climate*, *13*, 4378–4392, doi:10.1175/1520-
769 0442(2000)013<4378:MTPIAS>2.0.CO;2.

Sobel, A. H., G. Bellon, and J. Bacmeister (2007), Multiple equilibria in a single-column model of the tropical atmosphere, *Geophys. Res. Lett.*, *34*, L22,804, doi: 10.1029/2007GL031320.

Thorncroft, C., and K. Hodges (2001), African easterly wave variability and its relationship to atlantic tropical cyclone activity, *J. Climate*, *14*(6), 1166–1179.

Tobin, I., S. Bony, and R. Roca (2012), Observational evidence for relationships between the degree of aggregation of deep convection, water vapor, surface fluxes, and radiation, *J. Climate*, *25*(20), 6885–6904.

Wang, S., and A. H. Sobel (2011), Response of convection to relative sea surface temperature: cloud-resolving simulations in two and three dimensions, *J. Geophys. Res.*, *116*, D11,119, doi:10.1029/2010JD015347.

Wang, S., and A. H. Sobel (2012), Impact of imposed drying on deep convection in a cloud-resolving model, *J. Geophys. Res.*, *117*(D2), D02112, doi:10.1029/2011JD016847.

Wang, S., A. H. Sobel, and Z. Kuang (2013), Cloud-resolving simulation of TOGA-COARE using parameterized large-scale dynamics, *J. Geophys. Res. Atmos.*, *118*(12), 6290–6301, doi:10.1002/jgrd.50510.

Wang, S., A. H. Sobel, A. Fridlind, Z. Feng, J. M. Comstock, P. Minnis, and M. L. Nordeen (2015), Simulations of cloud-radiation interaction using large-scale forcing derived from the CINDY/DYNAMO northern sounding array, *J. Adv. Model. Earth Sys.*, *7*(3), 1472–1498.

Wing, A. A., and T. W. Cronin (2016), Self-aggregation of convection in long channel geometry, *Quarterly Journal of the Royal Meteorological Society*, *142*(694), 1–15, doi: 10.1002/qj.2628.

Wing, A. A., and K. A. Emanuel (2013), Physical mechanisms controlling self-aggregation of convection in idealized numerical modeling simulations, *J. Adv. Mod. Earth Sys.*, *5*, 1–14, doi:10.1002/2013MS000269.

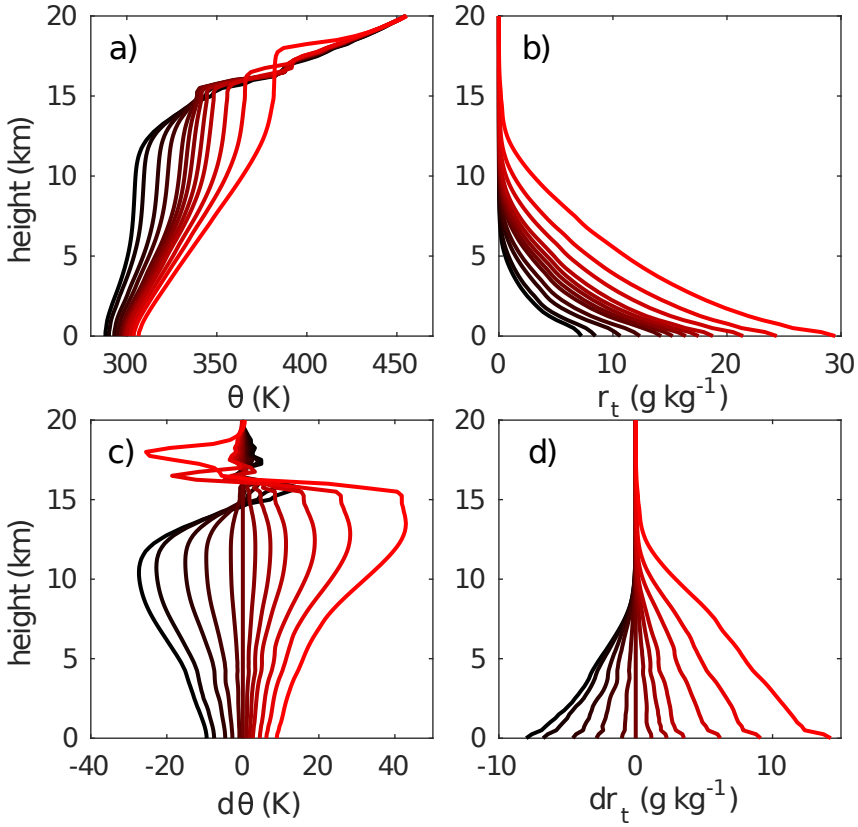

Figure 1. RCE profiles of (a) potential temperature, (b) total water vapor mixing ratio, (c) potential temperature anomaly relative to the 300 K SST, and (d) total water vapor mixing ratio anomaly relative to the 300 K SST reference profile, for SSTs ranging from 290 K (black) to 310 K (red).

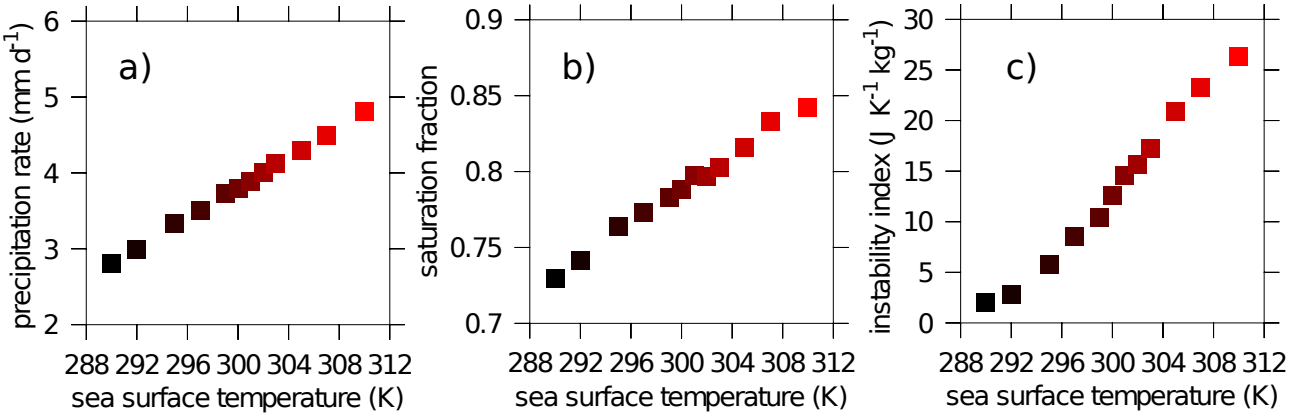

Figure 2. RCE (a) precipitation rate, (b) saturation fraction, and (c) instability index, for SSTs ranging from 290 K (black) to 310 K (red).

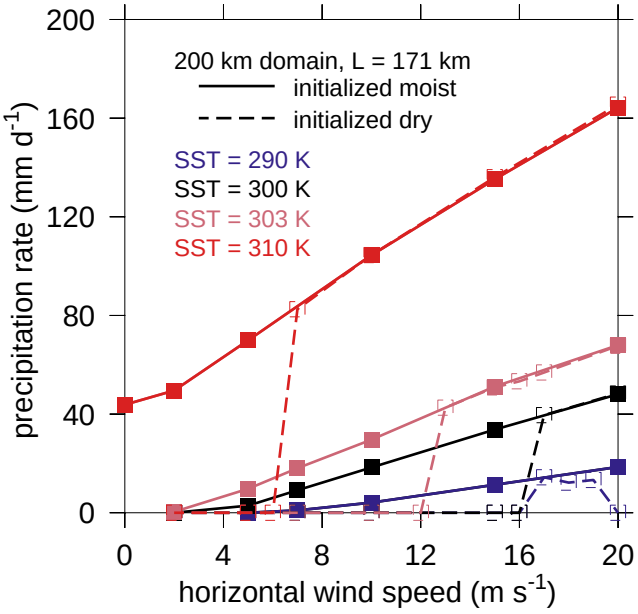

Figure 3. Precipitation rate versus horizontal wind speed for WTG simulations at different SSTs. For each SST, reference profiles of potential temperature and water vapor mixing ratio are calculated from the RCE simulations at the same SST. Each simulation is initially dry (dashed line, empty symbols) or moist (solid line, solid symbols).

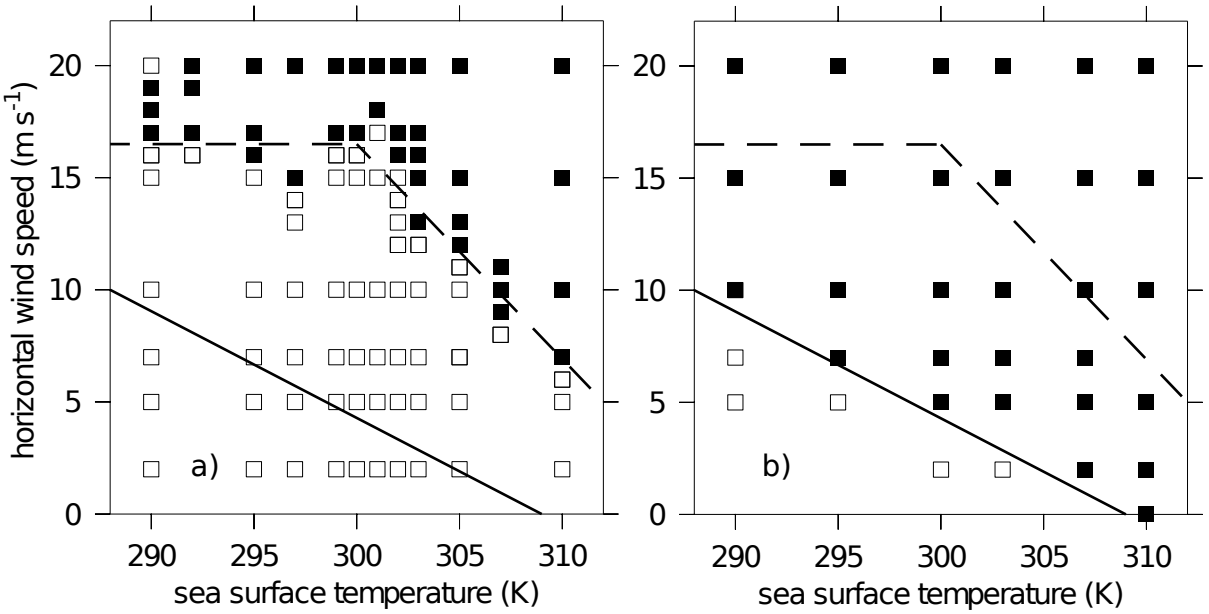

Figure 4. Precipitating (solid symbols) and non-precipitating (empty symbols) WTG simulations as a function of SST and horizontal wind speed, for a (a) dry, and (b) moist initialization. The dashed and solid lines are eye-guides separating three regions: below the solid line exists a single non-precipitating equilibrium, between the solid and the dashed lines is a region of multiple equilibria in precipitation, while above the dashed line exists a single precipitating equilibrium.

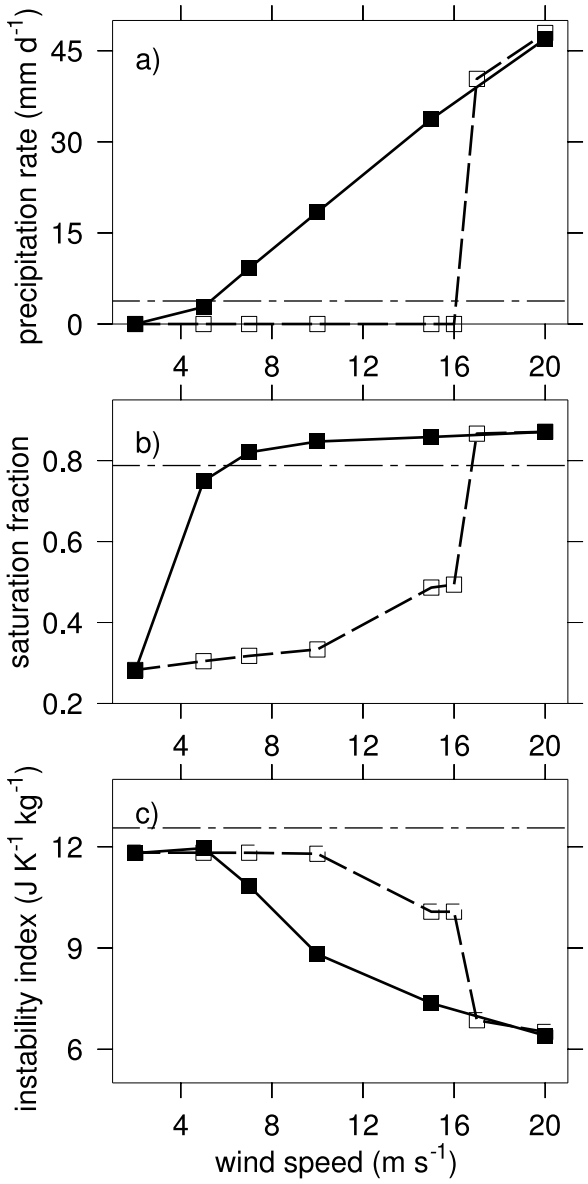

Figure 5. (a) Precipitation rate, (b) saturation fraction, and (c) instability index, versus horizontal wind speed, for the 300 K SST. The dashed line and empty symbols correspond to dry initialized, and the solid line and solid symbols correspond to moist initialized WTG simulations. The dash-dotted line corresponds to the RCE values of saturation fraction (b), and instability index (c).

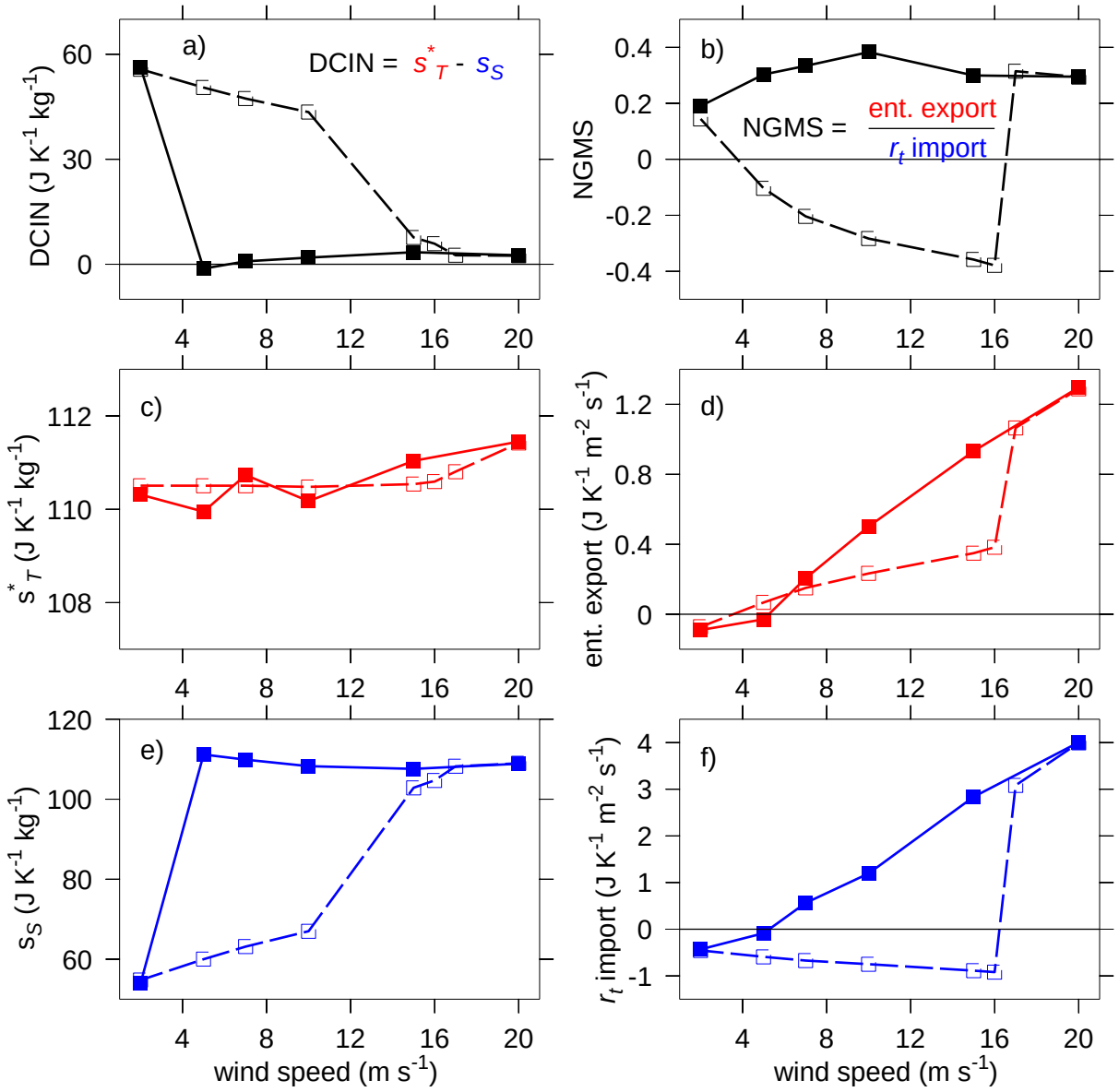

Figure 6. (a) DCIN, (b) NGMS, (c) threshold saturated moist entropy (s^*_T from equation 3), (d) WTG lateral entropy export (S_e from equation 4), (e) boundary layer moist entropy (s_S from equation 3), and (f) WTG lateral mixing ratio import (S_r from equation 4). The dashed line and empty symbols correspond to dry initialized, and the solid line and solid symbols correspond to moist initialized WTG simulations.

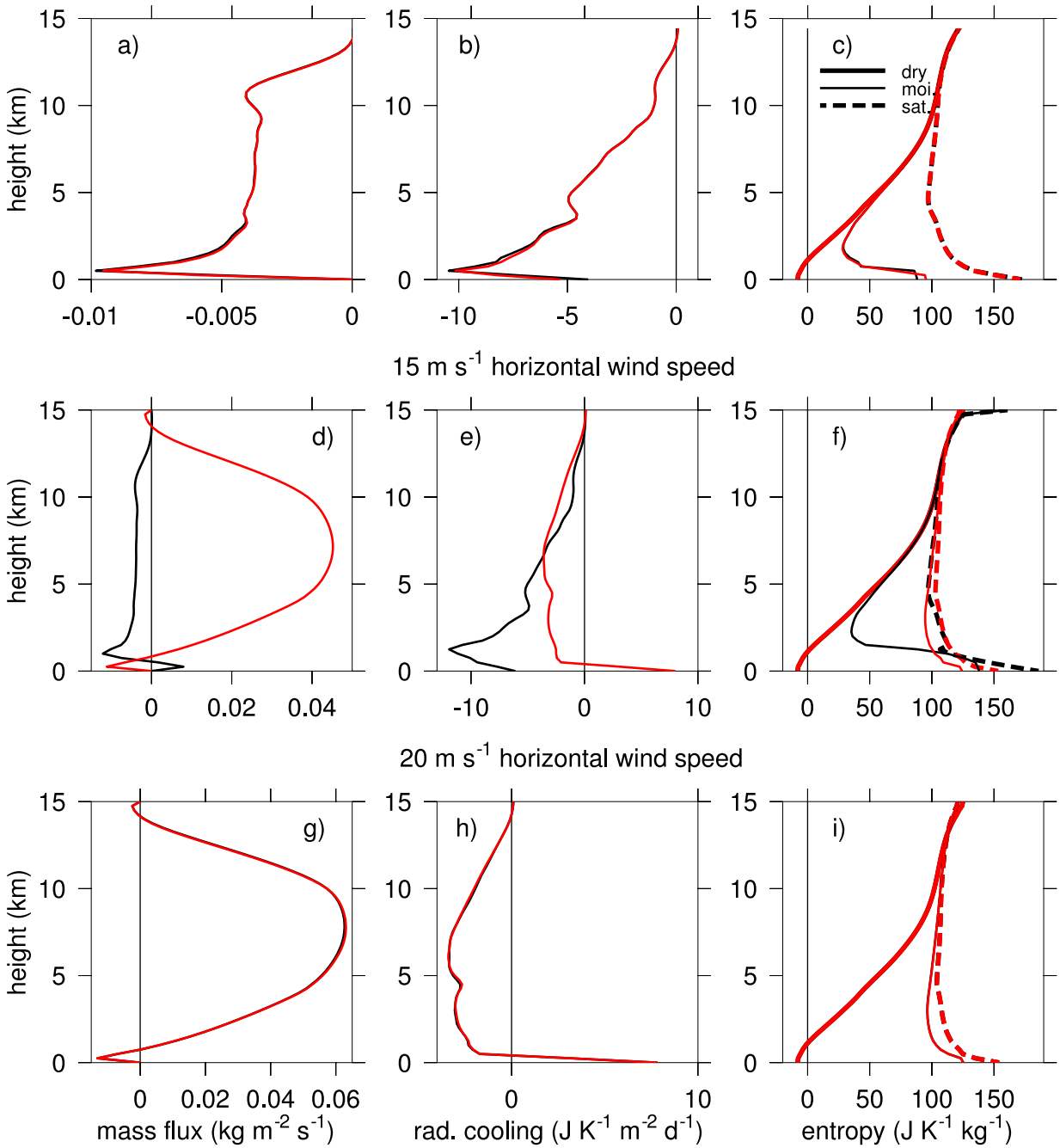

Figure 7. Mass flux (a, d, and g), radiative cooling (b, e, and h), and entropy (dry, moist, and saturated; c, f, and i), for WTG simulations with a 300 K SST, and 2 m s^{-1} (a–c), 15 m s^{-1} (d–f), and 20 m s^{-1} (g–i) wind speeds; dry initialized in black, and moist initialized in red. Note that in panels (a), (b), (c), (g), (h), and (i), the dry and moist initialized WTG simulations overlap.

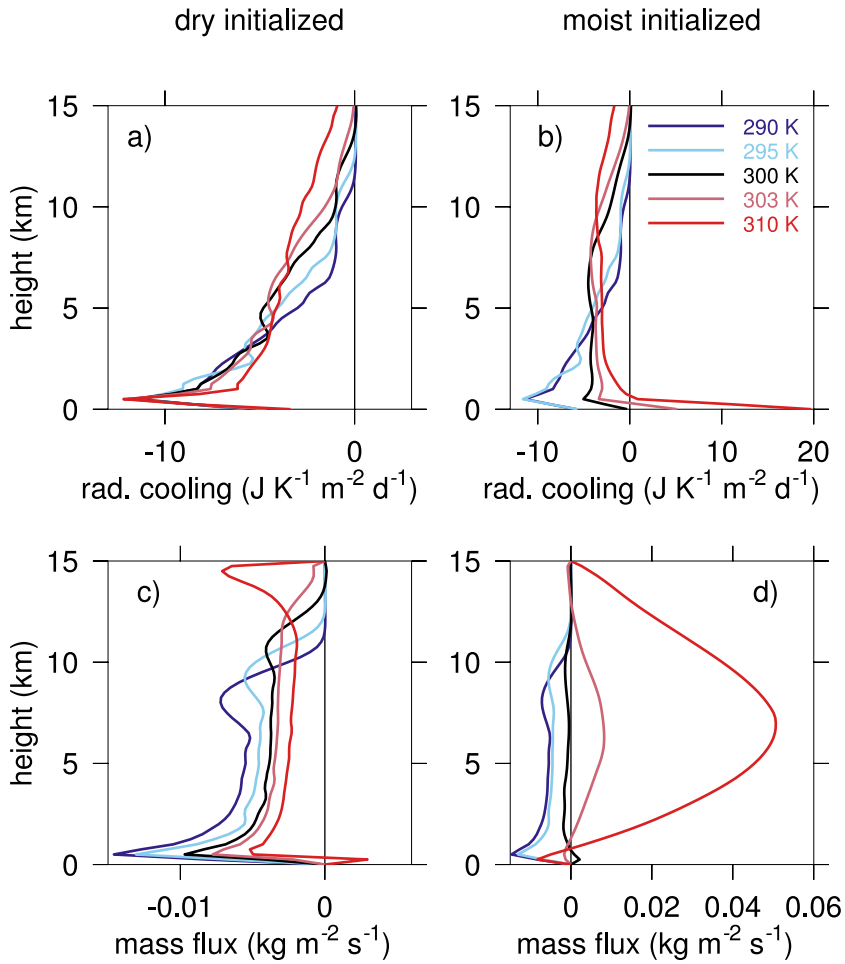

Figure 8. Vertical profiles of (a–b) radiative cooling, and (c–d) mass flux, for dry initialized (a and c), and moist initialized (b and d) simulations at 5 m s^{-1} wind speed. The SST legend is shown in panel b. Note that precipitating simulations occur at 300, 303, and 310 K SST in panels b and d (i.e. see figure 4 at 5 m s^{-1}.)

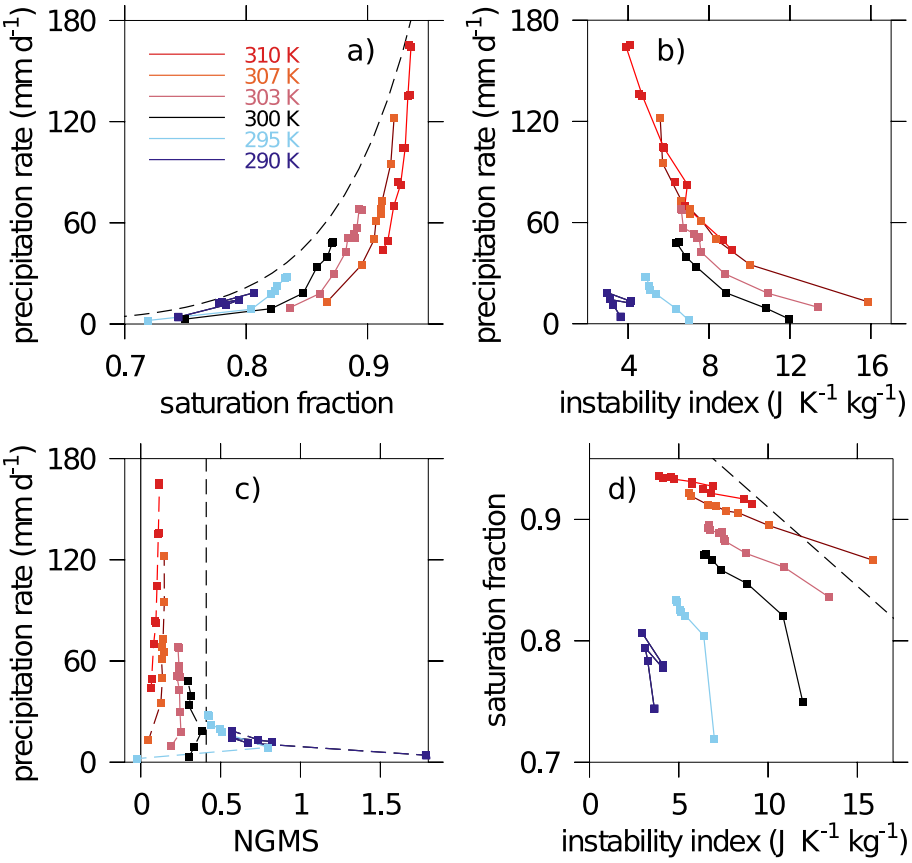

Figure 9. Precipitation rate versus (a) saturation fraction, (b) instability index, and (c) NGMS; and (d) saturation fraction versus instability index, for different SSTs (color legend is shown in panel a). The lines connect precipitating simulations for a given SST, while for the same SST the individual points correspond to different wind speeds. Panels a, c, and d also show relationships from previous research (dashed lines) for comparison: (a) the precipitation rate versus saturation fraction (SF) from *Bretherton et al.* [2004], $P = \exp[15.6(SF - 0.603)]$, (c) characteristic NGMS from DYNAMO observations [*Sentić et al.*, 2015], $NGMS_c = 0.41$, and (d) the saturation fraction versus instability index (II) from DYNAMO observations [*Sentić et al.*, 2015], $SF = -0.013II + 1.04$.

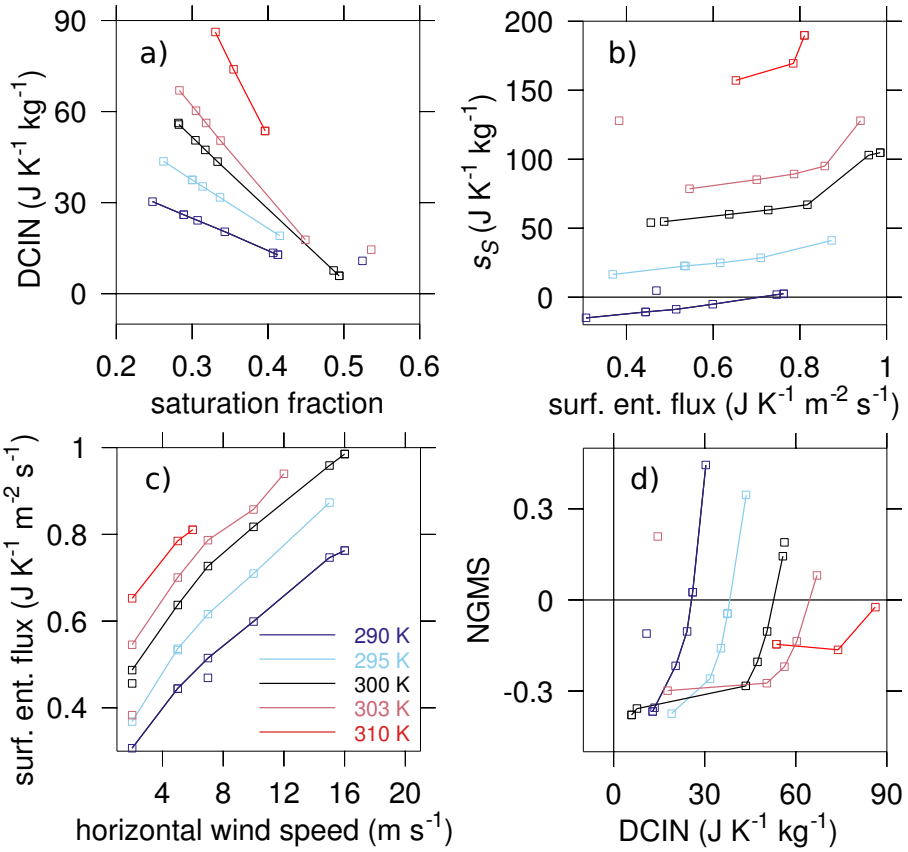

Figure 10. (a) DCIN versus saturation fraction, (b) mean moist entropy averaged in a layer between 0 and 1750 m (s_S from equation 3) versus surface entropy flux, (c) surface entropy flux versus the horizontal wind speed, and (d) NGMS versus DCIN, for different SSTs (color legend is shown in panel c), for non-precipitating simulations only. Only dry initialized simulations are connected with a line.

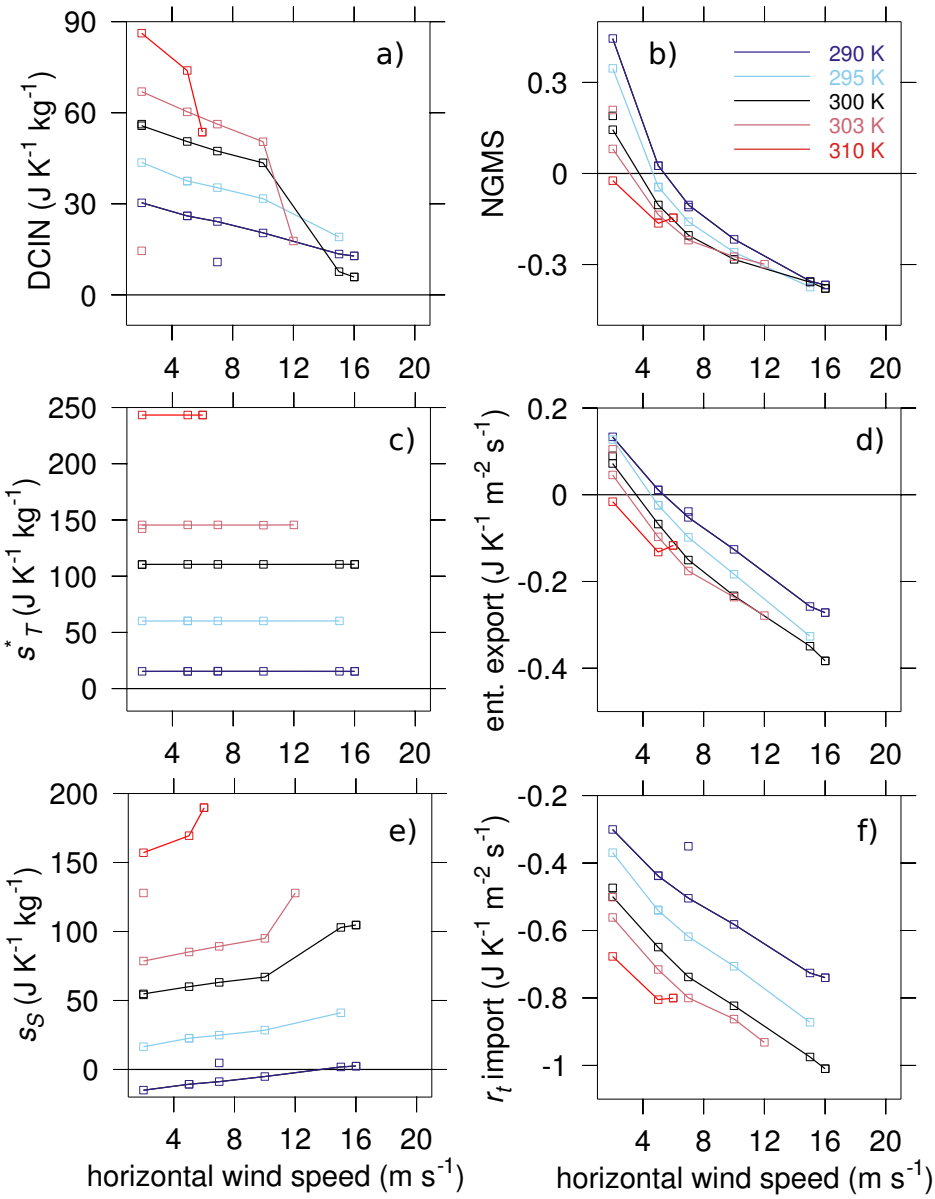

Figure 11. (a) DCIN, (b) NGMS, (c) threshold saturated moist entropy (s_T^* from equation 3), (d) WTG lateral entropy export (S_e from equation 4), (e) boundary layer moist entropy (s_S from equation 3), and (f) WTG lateral mixing ratio import (S_r from equation 4) versus horizontal wind speed, for different SSTs (color legend is shown in panel b), for non-precipitating simulations.

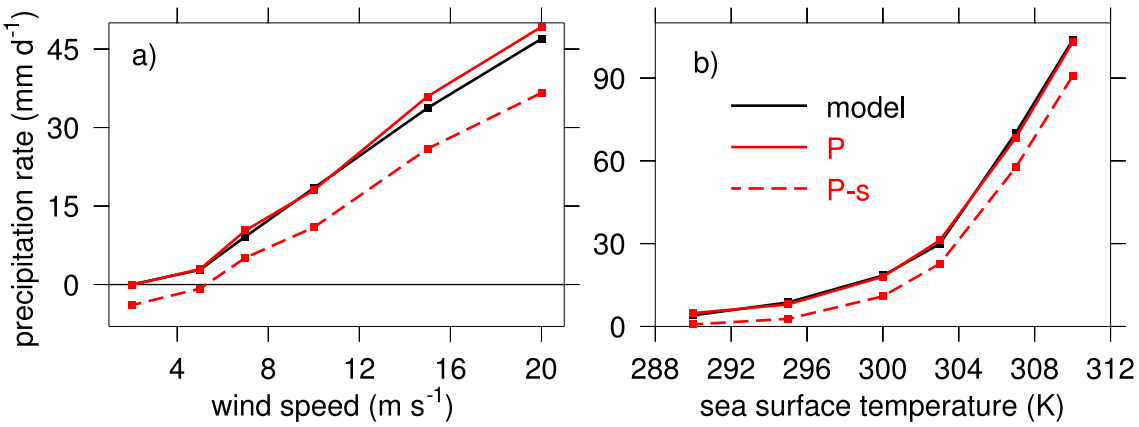

Figure 12. Precipitation rate versus (a) wind speed for a 300 K SST, and (b) SST for a 10 m s^{-1} wind speed, for the WTG simulations (black), and a simple precipitation model from equation A2 with surface fluxes (solid red) and without surface fluxes (dashed red).